Mesoporous Scaffolds Based on TiO_2 Nanorods and Nanoparticles for Efficient Hybrid Perovskite Solar Cells

Nazifah Islam[1], Mengjin Yang[2], Kai Zhu[2*], and Zhaoyang Fan[1*]

[1] Department of Electrical and Computer Engineering and Nano Tech Center, Texas Tech University, Lubbock, Texas, 79409, USA

[2] Chemistry and Nanoscience Center, National Renewable Energy Laboratory, Golden, Colorado 80401, USA

* Contact email: kai.zhu@nrel.gov; zhaoyang.fan@ttu.edu

Abstract

In a mesoporous hybrid perovskite solar cell (PSC), the mesoporous scaffold plays key roles in controlling the crystallization of perovskite material and charge carrier transport, and hence is critical for developing high efficient PSCs. Here we report the study of blending micrometer-long TiO_2 nanorods (NRs) into the commonly used nanoparticles (NPs) to optimize the mesoporous structure, with the aim of enhancing the perovskite material loading and connectivity as well as light harvesting. It was found that with 5%-10% of NRs incorporation, a uniform scaffold can be spin-coated and the PSC performance was improved. In comparison to the pure NP-based device, the power conversion efficiency was increased by about 27% when 10% NR was incorporated, due to enhanced light harvesting and charge collection. However, with more NRs blending, a homogeneous scaffold cannot be formed, resulting in PSC performance degradation. These findings contribute to a better design of mesoporous scaffolds for high-performance PSCs.

Introduction

Organometal halide based PSCs are attracting intensive interests towards developing new generation of photovoltaic (PV) technologies.[1-4] In the organic-inorganic hybrid perovskite material, the organic component renders the material with solution-processing capability and facilitates self-assembly for crystallization, while the inorganic component forms an extended framework through covalent/ionic bonds, which enables the preservation of a precise crystal structure in the film, ensuring good optoelectronic properties.[5,6] Such hybrid photoactive materials are promising to develop PV technology that combines the merits of cost-effective production of organic PV and high efficiency of inorganic PV.

The efficiency of PSC has been dramatically improved in the past few years with power conversion efficiency of ~ 20% demonstrated. This puts PSC technology potentially competing directly with the traditional semiconductor thin-film and even crystalline Si PV technologies. Nevertheless there are still enough rooms for further study and improvement. One aspect is related to the commonly used mesoporous scaffold structure. Of the two basic types of PSC device structures,[7,8] although planar PSCs have a simpler structure, the best certified power conversion efficiency has been limited to the mesoporous device structure.[9,10] In contrast to the planar film formation, the scaffold (e.g., TiO_2 nanostrutures) used in the mesoporous device can greatly facilitate the nucleation and growth of perovskites and avoid the fomation of pinholes to suppress internal device shunting. In addition, the mesoporous TiO_2 scaffold seems to have effect in suppressing the hysteresis behavior that is generally more severe in the planar structure.[11-13] Therefore, as alternatives to the commonly used TiO_2 nanoparticle (NP) based scaffold, other nanostructured electron tranport materials, such as vertically alligned TiO_2 nanorods,[14-17] 3D TiO_2 nanowires[18,19] or dendrites[20], TiO_2 nanotubes,[21] and ZnO nanowires[22-24] have been investigated.

Most of these efforts emphasized the enhanced electron transport in an aligned wire or tube based scaffold structure, similar as those for dye-sensitized solar cells.[25-28] However, the scaffold of PSCs plays roles other than just for electron transport. Therefore, engineering the scaffold and comparing their performance will benefit the further development of high-performance PSCs.

A typical mesoporous PSC structure is illustrated in Fig. 1(a). The mesoporous scaffold controls the photoactive perovskite layer formation by allowing the infilitration of precursor solution and confining the perovskite crystallites in the tiny volume of nanoporoes. It is important that the infiltrated perovskite forms continuous network in the scaffold by avoiding voids or dead volumes so that photon-generated electrons and holes both can be collected. This is not only critical for holes since they must be transported through perovskite to the hole transport material (HTM), but also useful for electrons. It is because electron injection into TiO_2 scaffold might be slow,[29] and a continuous perovskite network in the scaffold may facilitate direct electron collection in addition to electron transport in the TiO_2 scaffold. Furthermore, the crystal properties of perovskite formed within a mesoporous structure might be different from the crystal formed without a porous scaffold.[30] The pore-filling with perovskite to reduce charge recombination from TiO_2 and HTM was also reported.[31] However, poor pore-filling by perovskite often occurs due to the convoluted nanoscale porous channels within the scaffold.[21] Therefore, further optimizing the scaffold structure may contribute to further improving of the PSC performance. The commonly used TiO_2 NPs scaffold is formed by spin-coating of NP colloids with a typical size of around 20 nm. As schematically illustrated in Fig. 1(b), such a NP-based scaffold could have a very tortuous pore connectivity and limited pore volume, prohibiting a large perovskite material loading and a well-connected perovskite network. In addition, to maintain a thin perovskite layer for efficient charge collection, photon management and light harvesting will be a second issue since the tiny

NPs cannot provide effective light scattering. It is envisioned that if larger size components are introduced into the NP based scaffold, these two issues, the pore volume and connectivity and photon management might be relieved. As illustrated in Fig. 1(c), when micrometer long nanorods (NRs) are blended with NPs, we expect the resulted scaffold should be better than the pure NP based.

Herein, a study is presented on structural modifications of the NP-based scaffold by blending TiO_2 NRs with NPs in different ratios. Solar cells were made on these porous scaffolds by infiltrating perovskite material. The structure property and PSC performance was characterized to investigate the effect of incorporating NRs into NPs on the PSC performance.

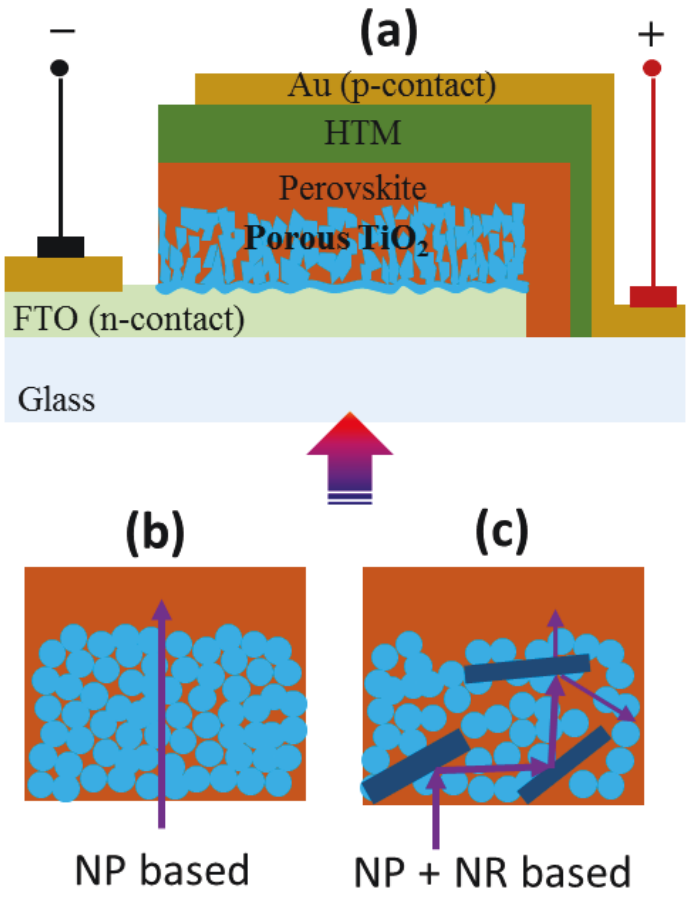

Figure 1. (a) Schematic of a typical mesoporous PSC structure fabricated on the florine-doped tin oxide (FTO) glass. It consists of FTO cathode, TiO_2 compact layer (C-TiO_2), TiO_2 mesoporous scaffold, infiltrated perovskite with a capping layer, HTM, and Au (or Ag) anode. Schematics, in a larger magnification, are also shown for cases of perovskite-infiltrated pure NP-based mesoporous scaffold in (b) and NP-NR-based scaffold in (c). Large pore volume and light scattering are emphasized in (c). The arrows in (b) and (c) represents light rays, emphasizing no significant light scattering in (b), while NRs can enhance light scattering in (c).

Experimental methods

TiO_2 NRs were synthesized hydrothermally from a 10M aqueous solution of NaOH and TiO_2 powders. In a typical process, 1g of Degussa P25 powder was added to 75mL NaOH solution in DI water and mixed thoroughly by stirring. The solution was transferred into a Teflon lined stainless steel autoclave of 100mL capacity and was kept at 200 ^oC for 72 hours in an electric oven. After cooling down, the product was washed in dilute HCl and then in DI water several times, followed by drying in vacuum for overnight. The produced long TiO_2 nanobelts or nanowire powder were further cut into short NRs by applying tip sonication in a solution. The shortened NRs were then dried and ground into fine powder. A solution of acetylacetone in water (1:10 v/v) was added to make a thick paste, which was further diluted by water. A few drops of Triton-X100 were added as surfactant. The NR paste, with a ratio of 5%, 10%, 25%, and 50%, was blended with TiO_2 NP paste to form the mesoporous scaffold. TiO_2 NP paste was diluted from screen printing paste[32] by adding ethanol to ~3.5 wt% TiO_2.

The PSC fabrication starts from coating a TiO_2 compact layer of about 20 nm on a patterned FTO glass substrate as detailed elsewhere.[33] The mesoporous scaffold was formed by spin-coating of the blended NP and NR paste. As a reference, PSC based on pure NP (0% NR) scaffold was also fabricated following the same procedures. Perovskite $CH_3NH_3PbI_3$ precursor was made of 1.4 M equimolar mixture of MAI and PbI_2 in γ-Butyrolactone (GBL, Aldrich)/dimethyl sulfoxide (DMSO, Sigma-Aldrich) (7/3 v/v). The substrate was spun at 4500rpm for 50s, and toluene was dispersed as an anti-solvent during the spinning. Perovskite film was further annealed at 85^oC for 10min. Hole transport material (HTM) was deposited on top of perovskite film by 4000 rpm for 30s using 2,2',7,7'-tetrakis(N,N-dip-methoxyphenylamine)-9,9'-spirobifluorene (Spiro-OMeTAD, Merck) solution, which consists of 80 mg Spiro-OMeTAD, 30 μl bis(trifluoromethane)

sulfonimide lithium salt (Li-TFSI) stock solution (500 mg Li-TFSI in 1 ml acetonitrile), 30 µl 4-tert-butylpyridine (TBP), and 1 ml chlorobenzene. Finally, silver metal film was thermally evaporated as a counter electrode.

The microstructures and crystal quality were characterized by scanning electron microscopy (SEM) and powder x-ray diffraction (XRD). The transmission and reflection of TiO_2 scaffolds without and with perovskite infiltration were measured to confirm the scattering effect of large feature size NRs. The PSC performance was characterized using a standard solar simulator. To qualitatively observe the impact of NR incorporation on the charge recombination rate in the subsequently infiltrated perovskite material, open-circuit photovoltage decay (OCVD) was measured for representative cells. The cell was illuminated by light emitting diodes (LEDs) to establish a steady state open-circuit voltage. After the illumination was switched off, the voltage decay was measured as a function of time.

Results and Discussion

Figure 2(a) shows the morphology of as synthesized TiO_2 nanostructure with a nanobelt or nanowire geometry. The tiny nanowires have a diameter down to nanometer scale, but nanobelts can have a width up to hundreds nanometers that may be considered as nanowire bundles. They have a length of tens of micrometers. In this alkaline solution based hydrothermal synthesis process, it is believed that the 3-D lattice structure of TiO_2 crystalline precursor was first disassembled by breaking down the Ti–O–Ti bonds.[34] The resulted TiO_6 octahedral share edges and vertices and rearrange into an opened 2-D framework, while sodium and hydrogen ions can fill into the interlayer voids, giving a generic structure of $Na_xH_{2-x}Ti_3O_7{\cdot}nH_2O$. Sodium-free hydrogenated

titanate was further obtained by ion-exchange reaction with acid in the HCl washing process.[35,36] When the hydrothermal reaction temperature is low, the very thin 2-D framework may wrap into tubular geometry to saturate dangling bonds and minimize the surface energy. At a higher temperature such as 200 ^{o}C used in this study, the rapid reaction kinetics leads to thicker sheets, giving nanobelt-like morphology that can be further split into nanowire shape.[37]

With a high aspect ratio, these long TiO_2 nanobelts cannot be dispersed in a spin-coating process to form a uniform mesoporous layer with a thickness of a few hundred nanometers, necessary for efficient PSCs. Therefore these as-synthesized TiO_2 nanobelts were cut into short NRs using tip sonication. As shown in Figure 2(b), the resulted NRs have a much reduced length of below one micrometer or so. X-ray diffraction (XRD) was employed to characterize their crystalline phases after annealing at 500^{o}C on FTO glass. As indicated in Fig. 2(c), these TiO_2 nanomaterials have the dominant anatase phase, although a small fraction of rutile phase inclusion does exist after annealing. The crystal phases and the respective planes of TiO_2 were identified according to JCPDS card number 21-1272 (anatase) and 21-1276 (rutile).

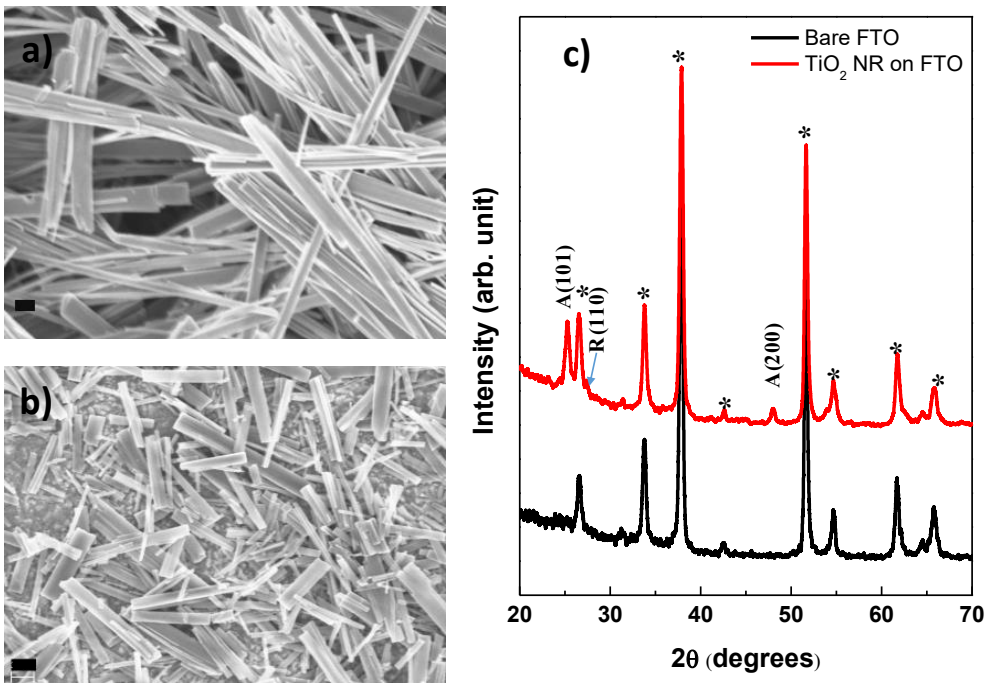

Figure 2. SEM images of long nanobelts/nanowires in (a) and short nanorods in (b). (Black scale bar: 300 nm). (c) XRD pattern of TiO_2 NRs dispersed on FTO glass substrate indicates the dominant anatase phase with tiny rutile inclusion. (*: peaks from FTO substrate. A: anatase, R: rutile).

By mixing these shortened TiO_2 NRs with ~20 nm NPs in different ratios, mesoporous scaffolds were coated onto FTO glass substrates that have a pre-coated TiO_2 compact layer. The inclusion of NRs will change the pore geometry and especially widen the nanopores. It is expected that wider pores would yield larger room to accommodate more perovskite crystals and also enhance their connectivity in the TiO_2 matrix.[38] SEM images in Figure 2 compare the surface morphology of these TiO_2 mesoporous layers. For a low ratio of NRs (5% and 10%), the included NRs are uniformly mixed and buried in the layer and therefore the film surface looks still uniform and comparable to that of pure NP based mesoporous layer. However, as NR concentration increases to 25% and especially to 50%, the surface of these scaffold layers has an unpredictable morphology that varies from clustered NRs to only NPs at different sites. At these high ratios, the layer may even lose continuity at some locations. The resulting morphology variations translate into a wide deviation in the layer thickness. Considering the micrometer length of these NRs and the less than ~ 200 nm thickness of the scaffold, it is not unexpected that at high ratio of NRs, the scaffold quality will be dramatically deteriorated. Similar observations were found from the cross-sectional SEM images of these structures (not shown here). Again, uniform scaffolds are observed for the first three structures (0%, 5%, and 10% NRs), while clusters and non-uniformity are the striking features for the last two structures (25% and 50% NRs) from cross-sectional images. The benefits of blending a small ratio of NRs into the scaffold can be observed by comparing the larger magnification images in Figure 3(a) and (c). Without deteriorating the scaffold integrity, a small amount of NRs can dramatically modify the porous structure by enlarging the pore volume and their connectivity.

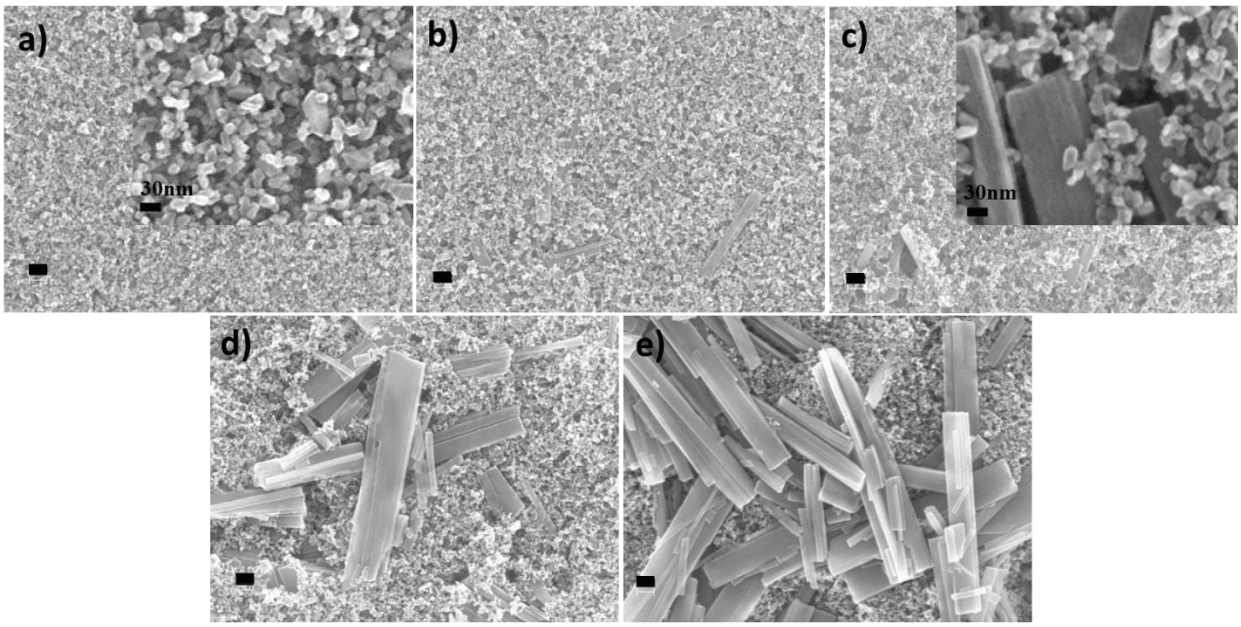

Figure 3. SEM images to compare surface morphology of the five porous TiO_2 scaffolds: a) pure NPs (0% NRs), b) 5% NRs, c) 10% NRs, d) 25% NRs, and e) 50% NRs. All images have a scale bar of 100 nm. The insets in a) and c) show the detailed surface morphology of 0% and 10% NR based scaffolds, respectively.

As the NRs possess a much larger feature size than NPs, at the scale of visible and near infrared light wavelength, we expect that the composite of NP and NR will scatter more strongly the incident light than pure NPs.[39] The diffusive transmission and reflection spectra, and the resulted absorption spectra of three representative mesoporous structures with infiltrated perovskite NR0%, NR10%, and NR50% were measured and they are presented in Figure 4. The related spectra of pure mesoporous layers are presented as Figure S1 in the Supplementary Information. As can be noticed, in term of diffusive transmission (Figure 4(a)), NR incorporation reduces the transmission in the longer wavelength range (~ 500 – 750 nm), and as more NR incorporated, the transmission reduction is more significant. For diffusive reflection (Figure 4(b)), although there is slight increase of reflection with NR incorporation at short wavelengths, *e.g.* the two small peaks at ~ 330 nm and ~ 380 nm, there is much more significant reflection suppression by NRs at longer wavelength (> ~ 650 nm). Considering both transmission and reflection, the absorption, as in Figure 4(c), is enhanced by NR incorporation, particularly in the longer wavelength range (> ~ 500 nm). It is noted that more NR incorporation will have more enhancement effect in term of light absorption. However, due to the integrity loss of the mesoporous layer for NR25% and NR50%, the subsequently infiltrated perovskite has very rough surface and low crystalline quality, as will be confirmed later.

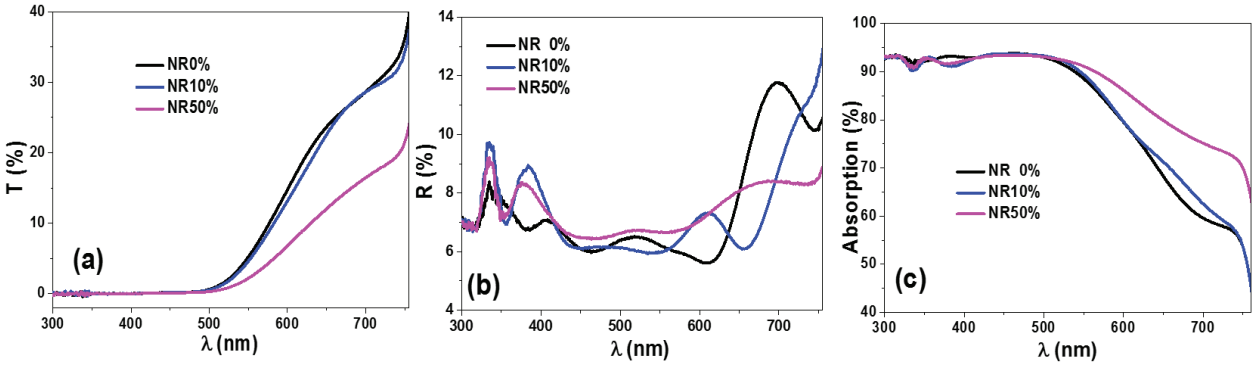

Figure 4. The transmission (a), reflectance (b), and absorption (c) of three representative samples NR0%, NR10%, and NR50% infiltrated with perovskite, were measured by an integrating sphere with light incidence from FTO glass side.

The mesoporous scaffolds were impregnated with $CH_3NH_3PbI_3$ perovskite photoactive material in a one-step spin-coating process, and the perovskite also formed a ~ 100 nm thick capping layer on the scaffold. The capping layer will greatly enhance light harvesting, and at the same time fully isolate the electron transporting scaffold from the subsequently coated HTM. A thin silver film was then deposited to finish the PSC fabrication. The cross-sectional SEM images of several representative cells are presented in Figure 5 (a-d). With the inclusion of NRs, the infiltrated porous layer looks more compact with fewer voids indicating greater pore-filling with perovskites. This will enhance the perovskite network connectivity, facilitating both hole and electron transport. For NR5% and NR10% based cells, the perovskite also forms a fairly uniform and continuous overlayer. However, for greater NR ratios (25% and 50%), the continuity and uniformity of the perovskite capping layer and also the HTM layer are abolished by the unfavorable morphology of the TiO_2 scaffold. The XRD pattern of the infiltrated perovskite material for 10% NR based scaffolds is presented in Figure 5(e), in conjunction with that of the compact layer (c-TiO_2) and the scaffold layer. The similar TiO_2 peaks are found from both the compact and porous films. In addition to those from substrate, all other peaks can be well indexed to perovskite $CH_3NH_3PbI_3$.[40] A strong perovskite (110) peak at 14.2º, smaller but significant (220) and (310) peaks at 28.2º and 31.9º, respectively, as well as the absence of PbI_2 peak at 12.5º, prove the complete conversion of PbI_2 and CH_3NH_3I precursors into $CH_3NH_3PbI_3$ perovskite and its high crystalline quality. In Figure 5(f), we compare the XRD pattern of perovskite on all five different scaffolds. The zoom-in plot of the dominant (110) diffraction peak is shown in Figure S2 in the Supplementary Information. These samples were measured under the same condition. The diffraction patters are the same, however, the perovskite diffraction intensity increases from sample NR0% to NR5% and NR10%, then decreases for NR25% and NR50% samples. For the

dominant (110) peak, their relative peak values are 1, 1.12, 1.38, 0.57 and 0.52, respectively. Considering that perovskite coating on the two scaffolds were implemented using the same recipe, the stronger diffraction intensity from NR 5% and NR10% samples suggests that after blending a small portion of NRs into the scaffold, the morphology change and pore widening resulted in more perovskite loading with better crystal quality and perovskite connectivity, which will enhance both the light harvesting and charge carrier collection. However, a large amount of NRs in samples NR25% and NR50% destroys the scaffold integrity, somehow resulting in deterioration of the perovskite crystalline quality, as noted from their low diffraction peak intensity and the peak widening.

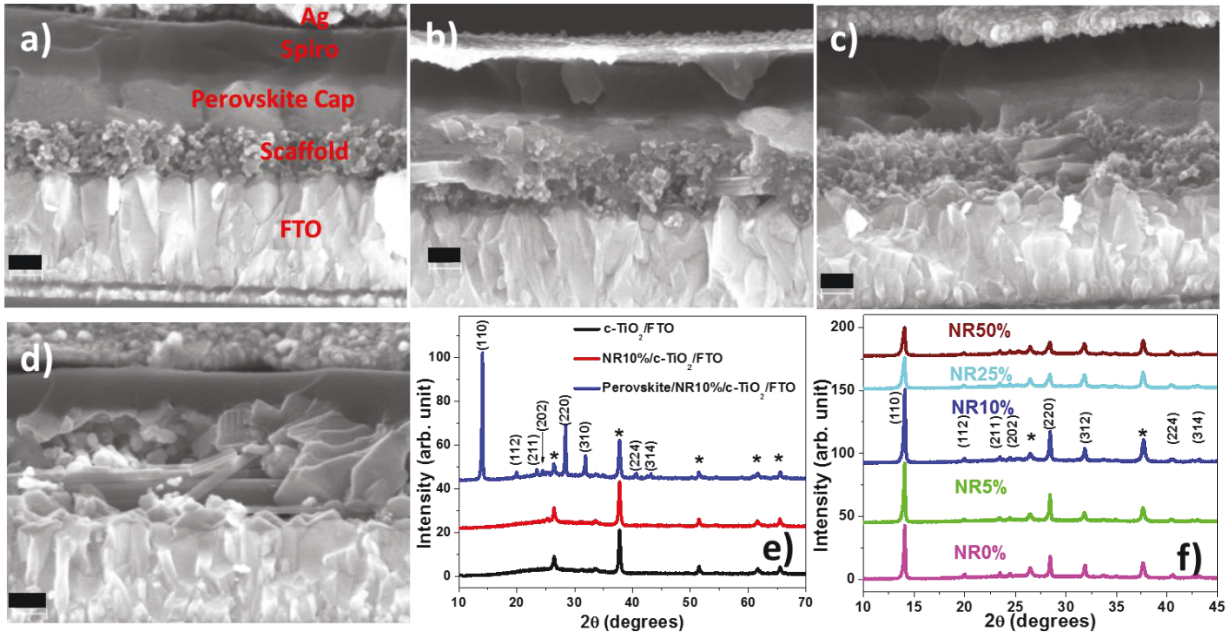

Figure 5: (a-d) Cross-section SEM of the fabricated PSCs based on scaffolds made of 0%, 5%, 10%, and 50% NR. (Black scale bar: 100 nm). (e) XRD pattern of the infiltrated perovskite material as well as those of the compact TiO_2 layer and a scaffold layer made up of 10% NR. (f) Comparison of the XRD patterns and diffraction intensities of perovskite formed on all five different scaffolds. (* represents FTO peaks).

The prepared PSCs with different NR composition in the mesoporous scaffold were characterized under a standard solar simulator illumination and the measured J-V curves are shown in Figure 6(a). The photovoltaic performance of these cells is summarized in Table 1. The PSC on 0% NR based scaffold exhibits a short circuit current density (J_{SC}) of 19.56 mA/cm^2, an open circuit voltage (V_{OC}) of 1.03 V, and a fill factor (*FF*) of 0.592, giving a power conversion efficiency (PCE) of 11.93%. This efficiency was improved to 13.88% when 5% NRs was blended into NPs to form the scaffold, and it was further boosted to 15.15% if 10% NRs was incorporated. Such a cell with 10% NR exhibited the best performance with a highest J_{SC} of 21.18 mA/cm^2, a highest V_{OC} of 1.06 V, and a largest *FF* of 0.675, resulting in 15.15% efficiency. However, further increasing the NR composition to 25% and 50%, the cell performance was dramatically degraded in terms of J_{SC}, V_{OC}, and *FF*. The much worse performance of the latter two devices is not a surprise considering the loss of uniformity in the scaffold layer as well as large backward reflection resulted from NR clustering. On the other hand, a small portion (5% and 10%) of NRs, when blended into NPs for scaffold without destroying its integrity, the photovoltaic performance does have considerable improvement, especially for J_{SC} and *FF*. As expected, the enhanced photocurrent could be attributed to greater perovskite loading and enhanced connectivity in the mesoporous scaffold that result in more photo carrier generation and facilitated electron and hole carrier transport when 5% and 10% NRs are incorporated, as well as light scattering introduced by NRs. For a comparable device configuration, the capturing of more perovskite material translates into ~ 4% and 8% increase of J_{SC} when 5% and 10% NRs were blended. More significantly, the facilitated charge carrier transport by the enhanced pore-filling results in ~ 11% and 14% increase of the PSC fill factor for these two devices. Overall, with 10% NR incorporation, a best photovoltaic performance was demonstrated, with the efficiency increased by 27%. The result suggests that

optimizing the mesoporous scaffold structure is a promising option in further improving the PSC efficiency.

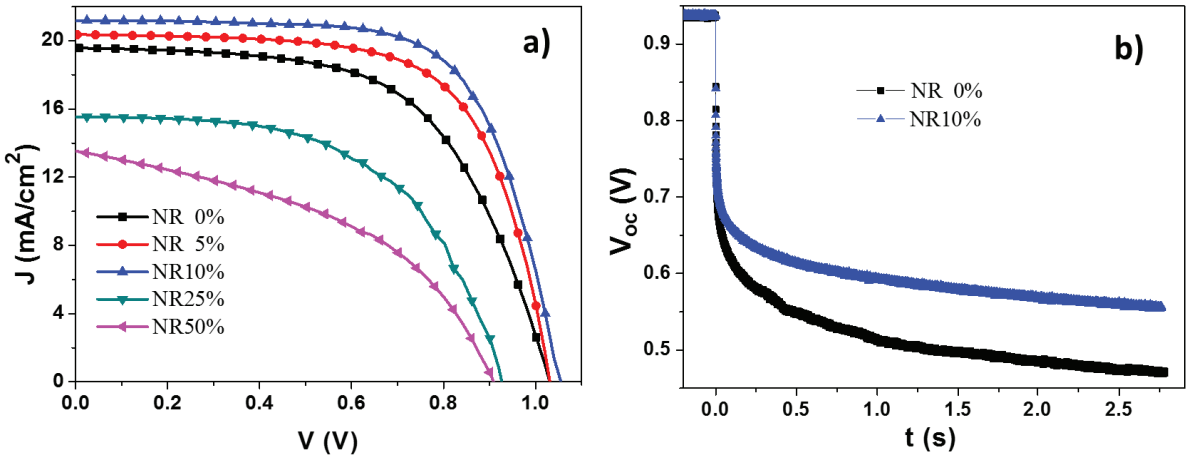

Figure 6: (a) J-V characteristic of the fabricated PSCs based on five different scaffold structures under one standard solar light illumination. (b) V_{OC} decay measurement for two representative cells. The monochromatic light illumination was turned off at t = 0.

Table 1: J-V measurement data of the solar cells.

	J_{sc} (mA/cm^2)	V_{oc} (V)	FF	PCE (%)
NR 0%	19.56	1.03	0.592	11.93
NR 5%	20.37	1.03	0.661	13.88
NR 10%	21.18	1.06	0.675	15.15
NR 25%	15.55	0.93	0.559	8.08
NR 50%	13.63	0.91	0.448	5.56

Enhancements of J_{SC} and FF of a solar cell could be caused by several factors related to the device fabrication. To confirm that such enhancement observed from NR5% and NR10% cells are due to better scaffold structure that gave better perovskite with reduced charge carrier recombination, the open-circuit photovoltage decay[41,42] for two representative cells, NR0% and NR10%, was measured. Here monochromatic LED illumination was set so that the obtained V_{OC} is closed to that under the standard one solar light. After switching off the illumination, V_{OC} decay was measured as a function of time, as presented in Figure 6(b). Initially, both cells have similar V_{OC} (~ 0.94 V). After 0.25 s, their V_{OC} decays to 0.70 V and 0.58 V, respectively. After 2.5 s, they are 0.56 V and 0.47 V. Both cells exhibits slower decay when compared to the literature[41,42]. However, here we emphasize that V_{OC} decay in NR10% cell is considerably slower than that of NR0% cell. This result confirms that after introducing small amount of NRs in the mesoporous scaffold to modify the porous structure, the subsequently infiltrated perovskite can have better crystal quality and better connection, facilitating both hole and electron transport and therefore suppressing the charge recombination.

Conclusion

This work presented a study on the effects of blending different ratios of TiO_2 nanorods into nanoparticles to form the mesoporous scaffold for hybrid perovskite solar cells. It was found that up to certain extent (~ 10%), the inclusion of nanorods contribute to large pore formation allowing greater perovskite loading, improved perovskite crystalline quality, enhanced perovskite connectivity in the scaffold while maintaining a fairly uniform morphology. The nanorods, with their large feature size, also enhance the perovskite light absorption through light scattering effect. Such improvement results in greater power conversion efficiency of the fabricated devices that

have reduced charge recombination rate. However, when NRs ratio is too larger, a favorable scaffold layer cannot be formed in the spin-coating process, leading to PSC performance degradation. The results of this study suggest that developing a novel porous architecture with large pores for perovskite accommodation as well as enhanced perovskite connectivity for efficient carrier transport is one effective option for developing better perovskite solar cells.

ACKNOWLEDGMENTS

Funding for the work at Texas Tech University from the National Science Foundation (CBET-1438681) is greatly acknowledged. M.Y. and K.Z. acknowledge the support from the U.S. Department of Energy SunShot Initiative under the Next Generation Photovoltaics 3 program (DE-FOA-0000990) for the work performed at the National Renewable Energy Laboratory (contract no. DE-AC36-08-GO28308).

Reference

1. H.-S. Kim, C.-R. Lee, J.-H. Im, K.-B. Lee, T. Moehl, A. Marchioro, S.-J. Moon, R. Humphry-Baker, J.-H. Yum and J. E. Moser, *Sci. Rep.*, 2012, **2**, 591.
2. M. Liu, M. B. Johnston and H. J. Snaith, *Nature*, 2013, **501**, 395-398.
3. J. Burschka, N. Pellet, S.-J. Moon, R. Humphry-Baker, P. Gao, M. K. Nazeeruddin and M. Grätzel, *Nature*, 2013, **499**, 316-319.
4. J. H. Noh, S. H. Im, J. H. Heo, T. N. Mandal and S. I. Seok, *Nano Lett.*, 2013, **13**, 1764-1769.
5. D. B. Mitzi, *Prog. Inorg. Chem.*, 2007, **48**, 1-121.
6. S. Luo, W. A. Daoud, *J. Mater. Chem. A*, 2015,**3**, 8992-9010.
7 Y. Zhao and K. Zhu, *J. Phys. Chem. Lett.*, 2014, **5**, 4175-4186.
8. T. Salim, S. Sun, Y. Abe, A. Krishna, A. C. Grimsdale and Y. M. Lam, *J. Mater. Chem. A***,** 2015,**3**, 8943-8969.
9. M. Grätzel, *Nat. Mater.*, 2014, **13**, 838-842.
10 NREL, Best Research-Cell Efficiencies, http://www.nrel.gov/ncpv/images/efficiency_chart.jpg, (accessed Auguest, 2015).
11 H. J. Snaith, A. Abate, J. M. Ball, G. E. Eperon, T. Leijtens, N. K. Noel, S. D. Stranks, J. T.-W. Wang, K. Wojciechowski and W. Zhang, *J. Phys.Chem. Lett.*, 2014, **5**, 1511-1515.
12 H.-W. Chen, N. Sakai, M. Ikegami and T. Miyasaka, *J. Phys. Chem. Lett.*, 2015, **6**, 164–169.
13. J. Wei, Y. Zhao, H. Li, G. Li, J. Pan, D. Xu, Q. Zhao and D. Yu, *J. Phys.Chem. Lett.*, 2014, **5**, 3937-3945.
14. J. H. Qiu, Y. C. Qiu, K. Y. Yan, M. Zhong, C. Mu, H. Yan and S. H. Yang, *Nanoscale*, 2013, **5**, 3245-3248.
15. H.-S. Kim, J.-W. Lee, N. Yantara, P. P. Boix, S. A. Kulkarni, S. Mhaisalkar, M. Grätzel and N.-G. Park, *Nano Lett.*, 2013, **13**, 2412-2417.
16. M. Yang, R. Guo, K. Kadel, Y. Liu, K. O'Shea, R. Bone, X. Wang, J. He and W. Li, *J. Mater. Chem. A*, 2014, **2**, 19616-19622.

17. Q. Jiang, X. Sheng, Y. Li, X. Feng and T. Xu, *Chem. Commun.*, 2014, **50**, 14720-14723.

18. K. Mahmood, B. S. Swain and A. Amassian, *Adv. Mater.*, 2015, **27**, 2859–2865.

19. Y. Yu, J. Li, D. Geng, J. Wang, L. Zhang, T. L. Andrew, M. S. Arnold and X. Wang, *ACS Nano*, 2015, **9**, 564-572.

20. W.-Q. Wu, F. Huang, D. Chen, Y. B. Cheng and R. A. Caruso, *Adv. Func. Mater.*, 2015, **25**, 3264-3272.

21. X. Gao, J. Li, J. Baker, Y. Hou, D. Guan, J. Chen and C. Yuan, *Chem. Commun.*, 2014, **50**, 6368-6371.

22. D. Bi, G. Boschloo, S. Schwarzmuller, L. Yang, E. M. J. Johansson and A. Hagfeldt, *Nanoscale*, 2013, **5**, 11686-11691.

23. M. H. Kumar, N. Yantara, S. Dharani, M. Graetzel, S. Mhaisalkar, P. P. Boix and N. Mathews, *Chem. Commun.*, 2013, **49**, 11089-11091.

24. D.-Y. Son, J.-H. Im, H.-S. Kim and N.-G. Park, *J. Phys. Chem. C*, 2014, **118**, 16567-16573.

25. K. Zhu , N. R. Neale , A. Miedaner , and A. J. Frank**,** *Nano Lett.*, **2007**, *7*, pp 69–74

26 X. Pan, C. Chen, K. Zhu, Z. Fan, Nanotechnology 22(23):235402, June 2011.

27. J. Villanueva-Cab, S.-R. Jang, A. F. Halverson, K. Zhu, and A. J. Frank, *Nano Lett.*, **2014**, *14*, pp 2305–2309

28 X. Feng, K. Zhu, A.J. Frank, C.A. Grimes, T.E. Mallouk, Angew. Chem., **2012**, 51, 2727–2730.

29. K. Wojciechowski, S. D. Stranks, A. Abate, G. Sadoughi, A. Sadhanala, N. Kopidakis, G. Rumbles, C.-Z. Li, R. H. Friend, A. K. Y. Jen and H. J. Snaith, *ACS Nano*, 2014, **8**, 12701–12709.

30. Y. Zhou, A. L. Vasiliev, W. Wu, M. Yang, S. Pang, K. Zhu and N. P. Padture, *J. Phys. Chem. Lett.*, 2015, **6**, 2292-2297.

31. T. Leijtens, B. Lauber, G. E. Eperon, S. D. Stranks and H. J. Snaith, *J. Phys. Chem. Lett.*, 2014, **5**, 1096-1102.

32. Y. X. Zhao, A. M. Nardes and K. Zhu, *J. Phys. Chem. Lett.*, 2014, **5**, 490-494.

33. Y. X. Zhao and K. Zhu, *J. Phys. Chem. C*, 2014, **118**, 9412-9418.

34. Y. Zhang, G. Li, Y. Jin, Y. Zhang, J. Zhang and L. Zhang, *Chem. Phys. Lett.*, 2002, **365**, 300-304.

35. Y. V. Kolen'ko, K. A. Kovnir, A. I. Gavrilov, A. V. Garshev, J. Frantti, O. I. Lebedev, B. R. Churagulov, G. Van Tendeloo and M. Yoshimura, *J. Phys.Chem.B*, 2006, **110**, 4030-4038.

36. E. Morgado, M. A. de Abreu, G. T. Moure, B. A. Marinkovic, P. M. Jardim and A. S. Araujo, *Chem. Mater.*, 2007, **19**, 665-676.

37. X. Pan, Y. Zhao, S. Liu, C. L. Korzeniewski, S. Wang and Z. Fan, *ACS Appl. Mater. Interfaces*, 2012, **4**, 3944-3950.

38. S. H. Hwang, J. Roh, J. Lee, J. Ryu, J. Yun and J. Jang, *J. Mater. Chem. A*, 2014, **2**, 16429-16433.

39. B. Tan and Y. Wu, *J. Phys. Chem. B*, 2006, **110**, 15932-15938.

40. N. J. Jeon, J. H. Noh, Y. C. Kim, W. S. Yang, S. Ryu and S. I. Seok, *Nat. Mater.*, 2014, **13**,897-903

41. A. Baumann, K. Tvingstedt, M. C. Heiber, S. Vath, C. Momblona, H. J. Bolink and V. Dyakonov, *APL Mater.* 2014, **2**, 081501.

42 A. Pockett, G. E. Eperon,T. Peltola, H. J. Snaith, A. Walker, L. M. Peter and P. J. Cameron, *J. Phys. Chem. C* 2015, **119,** 3456−3465**.**